Syntheses, Crystal Structures, and Magnetic Properties of $Sc_{19}Br_{28}Z_4$ Compounds with Z = Mn, Fe, Ru, or Os. Structural and Bonding Trends in $R_{16}X_{20}Z_4$-Type Oligomers

Sharon J. Steinwand and John D. Corbett*

Department of Chemistry, Iowa State University, Ames, Iowa 50011

James D. Martin

Department of Chemistry, North Carolina State University, Raleigh, North Carolina 27695

Received July 17, 1997[⊗]

The title compounds are obtained from reactions of the appropriate proportions of Sc, $ScBr_3$, and elemental Z in sealed Nb tubing at 800−900 °C. The structures with Z = Mn, Ru, Os were established by single crystal means to be Sc-deficient examples of the $Gd_4I_8^{4+}(Gd_{16}I_{20}Mn_4^{4-})$ structure (cubic $P\bar{4}3m$, $Z = 1$, $a = 10.941(9)$, 10.9897(5), 11.0032(3) Å) with 3.6(1), 3.0(1), and 2.9(1) scandium atoms in the tetrahedral cation portion, respectively. The cation deficiency with Z = Ru, Os affords 61-electron $Sc_{16}Br_{20}Z_4$ oligomeric units relative to the closed-shell expectation of 60 e^-. The dimensions, proportions, and bond orders in the $Sc_{16}Br_{20}Z_4$ oligomers (S_4 symmetry) are compared with those in the four yttrium and one gadolinium examples previously known in this or other structure types. The Sc−Mn combination again displays the longest Sc−Z distances. A systematic breathing distortion of $R_{16}X_{20}Z_4$ clusters that increases in the order Y−I, Y−Br, Sc−Br(Ru,Os,Ir) to Sc−Br−Mn and Gd−I−Mn parallels many other comparisons. Extended Hückel MO calculations show these variations depend not only on relative atom sizes but also on appreciable variations in orbital energies and the resulting R−Z mixing in the frontier cluster orbitals (Köckerling and Martin, unpublished). Unusual variations in the magnetic susceptibilities of the Ru, Os examples over the range of 6−300 K are shown to be fit very well by a model based on a Boltzmann distribution of the odd electron between close-lying frontier a_1 and t_1 orbitals with a temperature-dependent energy separation.

Introduction

An unusual family of $R_{16}Z_4X_{36}$ clusters has been observed among the many interstitially-stabilized rare-earth metal halides. These can be viewed as the oligomeric products of edge-sharing tetrahedral (2 + 2) condensation of classical octahedral $R_6(Z)X_{12}$-type clusters in which R is a rare-earth element, X is a halogen (fluorine excluded), and Z is a transition metal that centers the "octahedra". The cluster core can also be viewed as a truncated (R_{12}) tetrahedron that is tetracapped by R on the hexagon faces and centered by a large tetrahedron of Z. The bonding of Z to R appears to be more important than that between Z. These units are sheathed by 36 halogen atoms bonded on faces, edges, and vertices of the $R_{16}Z_4$ units, with most of the halogens being bifunctional and shared between clusters. The oligomers all have close to tetrahedral symmetry, but the packing and halide bridging in known examples reduce them to D_{2d}, D_2, or S_4 symmetry.

The stability and diversity of the oligomeric building blocks are attested to by the variety of structure types that contain these basic units and the range of elements that may be incorporated into these macroclusters. One structural family occurs for $Y_{16}I_{20}Ru_4$,[1] $Y_{16}Br_{20}Ru_4$, $Sc_{16}Br_{20}Fe_4$, and $Sc_{16}Br_{20}Os_4$.[2] The electron-richer interstitial Ir can also be incorporated in the isoelectronic $Y_{16}Br_{24}Ir_4$ by compensation in the form of four more bromide atoms, and the same unit interbridged by $Y^{III}Br_{6/2}$ chains is also found in a third structure type, $Y_{20}I_{36}Ir_4$ ($=Y_{16}Br_{24}Ir_4{\cdot}4YBr_3$). All of these have 60 skeletal electrons bonding the metal framework.[2]

Another version of oligomeric clusters was one of the earliest discoveries of this type, $Gd_{20}I_{28}Mn_4$.[3] Here, very similar $Gd_{16}I_{20}Mn_4$ clusters are tetrahedrally interbridged with smaller Gd_4I_8 cluster units, these both showing full T_d symmetry in space group $P\bar{4}3m$. Surprisingly, no further examples containing this unusual arrangement has been recognized in yttrium chloride, bromide, or iodide systems or elsewhere until the present study of the scandium bromides (although powder patterns of unidentified products often remain after many explorations).

Prior scandium studies have dealt almost entirely with the chlorides and iodides. Several novel reduced scandium chlorides have been prepared, including condensed cluster chain phases like Sc_4Cl_6B, Sc_5Cl_8C, and $Sc_7Cl_{10}C_2$, but only one type with isolated clusters, $Sc_7Cl_{12}Z$ (Z = B, C, N).[4,5] On the other hand, iodide systems have provided a couple of unique compounds like $Sc_6I_{11}C_2$[6] as well as more $Sc_7I_{12}Z$-type cluster phases (Z = B, C, Co, Ni).[7,8] The smaller chlorine thus has afforded more structural diversity, while iodine has allowed the incorporation of 3d transition metals as interstitials. The stability of many solid state compounds seems quite dependent on the sizes of the atoms and efficient packing, so it was thought possible that new rare-earth metal cluster phases would exist with the intermediate-sized bromine, as is the case with the singular R_4Br_4Os (R = Y, Er) with chains of centered, square antiprismatic clusters.[9] Although this idea was not helpful with

[⊗] Abstract published in *Advance ACS Abstracts,* December 15, 1997.

(1) Payne, M. W.; Ebihara, M.; Corbett, J. D. *Angew. Chem., Int. Ed. Engl.* **1991**, *30*, 856.
(2) Steinwand, S. J.; Corbett, J. D. *Inorg Chem.* **1996**, *35*, 7056.
(3) Ebihara, M.; Martin, J. D.; Corbett, J. D. *Inorg. Chem.* **1994**, *33*, 2079.
(4) Hwu, S.-J.; Corbett, J. D. *J. Solid State Chem.* **1986**, *64*, 331.
(5) Hwu, S.-J.; Corbett, J. D.; Poeppelmeier, K. R. *J. Solid State Chem.* **1985**, *57*, 43.
(6) Dudis, D. S.; Corbett, J. D. *Inorg. Chem.* **1987**, *26*, 1933.
(7) Dudis, D. S.; Corbett, J. D.; Hwu, S.-J. *Inorg. Chem.* **1986**, *25*, 3434.
(8) Hughbanks, T.; Corbett, J. D. *Inorg. Chem.* **1988**, *27*, 2022.

S0020-1669(97)00881-1 CCC: $14.00 © 1997 American Chemical Society

Table 1. Some Crystallographic and Refinement Data for $R_{\sim 19}Br_{28}Z_4$ Phases

empirical formula	$Sc_{4.72(3)}Br_7Os$	$Sc_{4.74(2)}Br_7Ru$	$Sc_{4.89(2)}Br_7Mn$
fw	962	873	834
space group, Z	$P\bar{4}3m$ (No. 215), 4	$P\bar{4}3m$ (No. 215), 4	$P\bar{4}3m$ (No. 215), 4
a[a] (Å)	11.0032(3)	10.9897(5)	10.941(9)
V (Å^3)	1332.2(1)	1327.26(6)	1310(1)
d_{calc} (g/cm^3)	4.795	4.37	4.23
μ (Mo Kα, cm^{-1})	325.5	242.2	244.1
R, R_w[b]	0.035, 0.034	0.042, 0.038	0.037, 0.043

[a] Dimensions from least squares analysis of Guinier powder data with Si as an internal standard; $\lambda = 1.540\,562$ Å, 22 °C. [b] $R = \sum||F_o| - |F_c||/\sum|F_o|$; $R_w = [\sum w(|F_o| - |F_c|)^2/\sum w(F_o)^2]^{1/2}$; $w = \sigma_F^{-2}$.

praseodymium,[10] it proved to be a useful and productive variation for yttrium[2] and for scandium, as follows.

Experimental Section

The sources of the high-purity metals utilized, the preparation of $ScBr_3$, the reaction techniques with welded Nb tubing, the refinement of lattice dimensions from Guinier patterns with the aid of Si as an internal standard, and the use of calculated patterns for the identification of products and the estimation of their yields (in terms of equivalent scattering powers) have been detailed before.[2]

Syntheses. Reactions in Sc−Br−Z systems proved to be very productive of new phases even though a fair number of these remain structurally uncharacterized. Synthetic attempts concentrated largely on the incorporation of transition metals as interstitials, namely, Cr−Cu, Ru, Rh, and Re−Pt, as well as C and B. Many reactions were heated slowly over a period of several days in an attempt to minimize the number of crystal nuclei formed and thereby to obtain larger, high-quality monocrystals. The inevitable ScOBr from traces of water was observed in all products in the form of light pink transparent blades that were often attached to the Nb tube walls. As usual, the use of higher temperatures or reloading products for further reaction resulted in larger amounts of the oxybromide, at least in part from dehydration of the fused silica jackets about the Nb containers.

Osmium as an interstitial yielded five new phases, three of which remain unidentified. A reaction loaded as Sc_4Br_5Os and heated at 950 °C for 2 weeks yielded approximately equal parts of $Sc_{19}Br_{28}Os_4$ and an unknown with an estimated composition near Sc_4Br_4Os. These two have very distinctive crystal habits, $Sc_{19}Br_{28}Os_4$ as black cubes or bricks and the unknown as long fibrous black needles. The less reduced composition $Sc_6Br_{11}Os$ reacted as above yielded mostly $Sc_{19}Br_{28}Os_4$ and $ScBr_3$. Several reactions were loaded on the composition $Sc_{19}Br_{28}Os_4$ and heated for 20 days or more. At 975 °C, the products were the same unknown and $ScBr_3$, at 900 and 850 °C, nearly quantitative yields of $Sc_{19}Br_{28}Os_4$ with a minute trace of the same unknown identified only visually, and at 800 °C, only $Sc_{19}Br_{28}Os_4$. A reaction loaded as $Sc_{16}Br_{20}Os_4$ and heated at 850 °C for 26 days produced ∼50% $Sc_{16}Br_{20}Os_4$ (isostructural with $Y_{16}Br_{20}Ru_4$[2] on the basis of its powder pattern), minor amounts of a second unknown, and $Sc_{11}Os_4$.[11] Addition of NaBr to the reaction produced, in addition to intermetallics and Na−Sc^{III}−Br ternary phases, a third unknown as black matted fibers that was stable at both 840 and 950 °C.

Ruthenium reactions loaded as Sc_4Br_5Ru and heated to 900 °C for 2 weeks produced well-formed cubes of $Sc_{19}Br_{28}Ru_4$ in addition to $ScBr_3$ and an unidentified phase. Similar reactions loaded as $Sc_{19}Br_{28}Ru_4$ produced >85% of the target phase, but further reaction at 975 °C decomposed this to starting materials. More metal-rich compositions heated at 950 °C also produced moderate amounts (∼30%) of two unidentified phases.

Exploratory syntheses in the Sc−Br−Fe system resulted in the preparation of $Sc_{19}Br_{28}Fe$ as well as the known $Sc_{16}Br_{20}Fe_4$. A reaction loaded as $Sc_{19}Br_{28}Fe_4$ and heated at 950 °C for 20 days gave >90% of this phase ($a = 10.9053(5)$ Å, $V = 1296.9(2)$ Å^3, 47 lines). More metal-rich reactions produced mixtures of mostly $Sc_{19}Br_{28}Fe_4$ with small amounts (≤20%) of $Sc_{16}Br_{20}Fe_4$ and, in the most reduced cases, Fe−Sc intermetallic phases. As observed before with Y−Br−Z systems,[2] the presence of NaBr in 840 °C reactions yielded one or more Na−Sc^{III}−Br phases that apparently acted as a flux and enhanced the formation of only $Sc_{16}Br_{20}Fe_4$.

In order to synthesize a scandium bromide analogous to $Gd_{20}I_{28}Mn_4$, reactions loaded at that stoichiometry were heated for a least 20 days at temperatures ranging from 725 to 950 °C. Those at 800 or 850 °C produced small to moderate (∼35%) amounts of black crystalline $Sc_{\sim 20}Br_{28}Mn_4$, a small amount of Mn_2Sc, and a large quantity of black fibrous material (commonly described as "mouse fur") whose powder pattern matched that reported for Sc_2Br_3.[12] Higher and lower temperatures resulted in only Sc_2Br_3 and Mn_2Sc. Addition of NaBr did not produce anything useful.

Reactions in the Sc−Br−Ir system produced three new but unknown phases. Those loaded as $Sc_6Br_{11}Ir$ and Sc_4Br_5Ir and heated at 950 °C for 2 weeks produced ∼25−50% of thin black fibrous needles plus $ScBr_3$ and IrSc. Oscillation photographs of these indicated a repeat of ∼9 Å along the needle direction, but the crystal qualities were poor. A slightly more metal-rich reaction run instead at 800 °C for 20 days gave the same plus a second unidentified phase in nearly equal yields, suggesting that the reaction temperature is a significant factor. A third unknown phase was formed when NaBr was added to the reaction. The powder patterns of the first and third unknowns matched the products of comparable osmium reactions (above), but satisfactory single crystals were again not found.

Similar reactions involving Co and Ni metals gave only the corresponding $Sc_7Br_{12}Z$[8] cluster phases in moderate to high yields plus binary intermetallic phases and an unidentified cobalt compound. The lattice parameters for the above Co and Ni compounds (space group $R\bar{3}$) were determined to be $a = 13.795(1)$, 13.795(2) Å and $c = 9.585(1)$, 9.493(1) Å, respectively, similar to those observed for the isostructural iodides.

Attempts to incorporate Cr, Cu, Rh, Re, or Pt as Z at 850 °C or higher yielded mostly $ScBr_3$ and intermetallics or unreacted Z along with unknowns with Pt and Re. A few attempts to incorporate B and C yielded several unknowns, $Sc_7Br_{12}C$,[7] and one boride with a powder pattern that closely resembled that calculated on the basis of the structure of $Sc_6I_{11}C_2$.[6]

Structure Determinations. A summary of some data collection and refinement parameters for all three structures studied is given in Table l. Data collection on a black cube from a reaction near a Sc_5Br_7Os composition was performed at room temperature on an Enraf-Nonius CAD-4 automated diffractometer using Mo Kα radiation. The random reflection search procedure yielded a primitive cubic unit cell, and the package programs indicated a $m\bar{3}m$ Laue class. One hemisphere ($\pm h,k,\pm$l) of data to $2\theta < 50°$ was followed by measurement of three ψ scans and the usual data reduction during which absorption was corrected with the aid of the average of these scans.

Intensity statistics strongly indicated a noncentrosymmetric space group, and since no extinction conditions were observed, space group $P\bar{4}3m$ was chosen. Direct methods (SHELXS-86) readily provided a solution with three Sc, three Br, and one Os atoms. Isotropic refinement (TEXSAN[13]) of the model gave a reasonable residual, but the thermal parameters were very small and even negative for the Os atom. Anisotropic refinement gave $R/R_w = 0.032/0.035$ but did not solve the

(9) Dorhout, P. K.; Corbett, J. D. *J. Am. Chem. Soc.* **1992**, *114*, 1697.
(10) Llusar, R.; Corbett, J. D. *Inorg. Chem.* **1994**, *33*, 849.
(11) Villars, P.; Calvert. L. D. *Pearson's Handbook of Crystallographic Data for Intermetallic Phases*, 2nd ed.; American Society for Metals International: Metals Park, OH, 1991; Vols. 3 and 4.
(12) McCollum, B. C.; Camp, M. J.; Corbett, J. D. *Inorg. Chem.* **1973**, *12*, 778.
(13) *TEXSAN*, version 6.0 package; Molecular Structure Corp.: The Woodlands: TX, 1990.

temperature factor problems. However, application of a spherical 2θ-dependent absorption correction and subsequent data reduction with the CHES program[14] yielded more reasonable thermal parameters and $R = 0.038$ on isotropic refinement. However, B for Sc3 was over three times those of the other Sc atoms. Refinement of the multiplicity of this site with B fixed indicated that the position was less than fully occupied by over 6σ. Refinement of both the thermal parameter and multiplicity of Sc3 gave a converged isotropic refinement, R/R_w = 0.037/0.035 and an occupancy of 72(3)%. Subsequent anisotropic refinement with this occupancy fixed proceeded smoothly to R/R_w = 0.035/0.034. The corresponding composition is $Sc_{18.9(1)}Br_{28}Os_4$. The largest peaks in the final difference Fourier map were +1.44 e/A^3, 1.00 Å from Os, and −l.10 e/A^3.

A crystal from a reaction loaded as Sc_3Br_5Ru was used for refinement of the ruthenide. The Laue determination again yielded $m\bar{3}m$. One octant (h,k,l) of data for the cubic cell was collected to $2\theta \leq 70°$ on a Rigaku AFC6R diffractrometer followed by measurement of three ψ scans for absorption correction. An initial model based on the atom positions from $Sc_{19}Br_{28}Os_4$ gave a smooth isotropic refinement, but the thermal parameter for Sc3 was again large. Refinement of both its multiplicity and thermal parameter gave a more reasonable value of the latter for Sc3, although it was still larger than for the other two Sc atoms. The isotropic result was $R/R_w = 0.051/0.062$, and the anisotropic refinement was uneventful and converged at R/R_w = 0.043/0.056. Anisotropic refinement of the isotropic result following the application of DIFABS[15] gave somewhat better absorption correction with more uniform ellipsoids, $R/R_w = 0.042/0.038$, and the refined composition $Sc_{18.96(8)}Br_{28}Ru_4$. The largest positive and negative peaks in the final difference Fourier calculation were +3.26 e/A^3, located 2.28 Å from Brl, and −2.26 e/A^3. However, the largest peaks in this map were located at higher symmetry sites and did not stand out from the background; rather, there was a relatively steady decrease in the intensity for other residual peaks. Lattice parameters for the above compounds were calculated from the respective Guinier powder pattern data by least squares using positions of 45 and 28 indexed lines and Si (NIST, National Institute of Standards and Technology) as an internal standard.

A single crystal study of the manganese compound utilized a black crystal from a reaction loaded as Sc_5Br_7Mn. The data were collected at room temperature on an Enraf-Nonius CAD-4 diffractometer to $2\theta = 56°$ followed by measurement of three ψ scans. The Laue class $m\bar{3}m$ was again indicated. The duplicate data with $I > 0$ averaged to 0.094 in space group $P\bar{4}3m$. The positional parameters for $Sc_{19}Br_{28}Os_4$ were used as an initial model. Isotropic refinement showed a thermal parameter for Sc3 that was twice that of Sc1 and Sc2 (R = 0.047), and refinement of the multiplicity and B together reduced the former to an 89(2)% occupancy. Anisotropic refinement with the Sc3 multiplicity varying as well gave the same result and R/R_w = 0.037/0.043 at convergence. The largest peaks in the ΔF map were +1.78 e/A^3, 0.87 Å away from Sc3, and −1.55 e/A^3. It is difficult to be certain that the partial occupancy is truly significant and not just an artifact of the refinement, especially considering the proximity of the small residual electron density near Sc3. The Sc3 would be expected to have a larger thermal parameter just on the basis of its environment within the structure. If the partial occupancy is taken as real, the refined composition is $Sc_{19.56(8)}Br_{28}Mn_4$, closer to that of the analogue $Gd_{20}I_{28}Mn_4$ than was found for the electron-richer Os and Ru examples. The less precise lattice parameter for this phase was calculated from 13 lines measured in the Guinier powder pattern of a multiphasic sample. Attempts to refine this structure as twinned (quadrilled) intergrowths of an ordered $R3m$ structure, in parallel with past studies on $Gd_{20}I_{28}Mn_4$,[3] were unsuccessful.

Powder patterns calculated from the refined parameters are in excellent agreement with observation for all three compounds; enantiomeric checks for all three did not yield significant differences. Tables of more extensive crystallographic data, anisotropic displacement parameters, and angles within all three structures are available in the Supporting Information. These and the F_o/F_c listing are also available from J.D.C.

Magnetic Susceptibilities. Magnetic susceptibilty measurements were performed on samples of $Sc_{19}Br_{28}Os_4$, $Sc_{19}Br_{28}Ru_4$, and $Sc_{19}Br_{28}Fe_4$, all of which appeared to be single phase by Guinier X-ray powder diffraction. Data were secured on two osmium samples to check the unusual behavior. No magnetic data was obtained for the manganese compound because it was not possible to obtain this phase in high yield. Weighed powdered samples (~35 mg) were loaded under He into an improved container in which the sample was held between the faces of two fused silica rods.[16] Data were collected over 6−300 K and at a field of 3 T with the aid of a Quantum Design MPMS SQUID magnetometer. The field dependencies of the magnetization between 0.1 and 5 T over a range of temperatures were measured for the Ru and Os compounds to screen for possible magnetic impurities. The Os sample showed a zero-field intercept of only 6.2×10^{-5} emu, whereas the Ru sample showed a considerably larger intercept of 1.3×10^{-3} emu, for which the data were corrected. Magnetization data as a function of the field were not measured for the iron sample; nevertheless, the large Weiss constant implied by the uncorrected data suggest that a significant correction for impurities is needed. All data were corrected for the susceptibility of the container and for the estimated core diamagnetism, -1.20×10^{-3}, -1.30×10^{-3}, and -1.17×10^{-3} emu/mol, respectively.

Table 2. Positional and Isotropic-Equivalent Thermal Parameters for Three $Sc_{\sim 19}Br_{28}Z_4$

atom	Wyckoff	x	y	z	B_{eq}[a]
		$Sc_{18.9(1)}Br_{28}Os_4$			
Os	4*e*	0.0973(1)	*x*	*x*	1.1782(4)
Sc1	12*i*	0.1169(3)	*x*	0.3286(4)	1.4(1)
Sc2	4*e*	−0.1386(5)	*x*	*x*	1.552(2)
Sc3[b]	4*e*	0.3840(4)	*x*	*x*	1.714(4)
Br1	12*i*	0.1274(1)	*x*	0.6027(2)	1.55(6)
Br2	12*i*	0.3651(1)	*x*	0.1259(2)	1.88(7)
Br3	4*e*	−0.3735(3)	*x*	*x*	2.55(1)
		$Sc_{19.0(1)}Br_{28}Ru_4$			
Ru	4*e*	0.0990(1)	*x*	*x*	0.3099(4)
Sc1	12*i*	0.1171(2)	*x*	0.3284(3)	0.57(6)
Sc2	4*e*	−0.1381(3)	*x*	*x*	0.376(1)
Sc3[c]	4*e*	0.3821(4)	*x*	*x*	0.915(2)
Br1	12*i*	0.1282(1)	*x*	0.6031(2)	0.83(4)
Br2	12*i*	0.3643(1)	*x*	0.1246(2)	1.12(4)
Br3	4*i*	−0.3739(2)	*x*	*x*	1.785(1)
		$Sc_{19.56(8)}Br_{28}Mn_4$			
Mn	4*e*	0.0900(3)	*x*	*x*	1.348(1)
Sc1	12*i*	0.1162(3)	*x*	0.3246(3)	1.04(7)
Sc2	4*e*	−0.1429(4)	*x*	*x*	1.422(2)
Sc3[d]	4*e*	0.3839(4)	*x*	*x*	1.698(2)
Br1	12*i*	0.1282(1)	*x*	0.6017(2)	1.13(4)
Br2	12*i*	0.3650(1)	*x*	0.1260(2)	1.47(4)
Br3	4*e*	−0.3705(2)	*x*	*x*	1.833(1)

[a] $B_{eq} = (8\pi^2/3)\sum_i\sum_j U_{ij} a_i^* a_j^* \vec{a}_i \vec{a}_j$. [b] Occupancy = 0.72(3). [c] Occupancy = 0.74(2). [d] Occupancy = 0.89(2).

Extended Hückel Calculations.[17] These were carried out using the suite of programs developed by R. Hoffmann and his co-workers at Cornell University. The halogen-sheathed units $[R_{16}X_{20}Z_4]X_{16}$ were modeled after the observed structures and included exo halogen at all vertex positions. The metal orbital energies H_{ii} obtained from charge-consistent interactions were as follows, in eV for d, s, p, respectively: Sc, −7.03, −7.18, −4.52; Y, −6.80, −7.02, −4.40; Gd, −7.34, −6.15, −3.05; Mn, −7.57, −7.24, −4.71; Ru, −8.18, −5.57, −2.61. The orbital exponents employed were the default values throughout.

Results and Discussion

Structures. The atom positional and isotropic-equivalent ellipsoid data for the refined structures and compositions of $Sc_{\sim 19}Br_{28}Z_4$ (Z = Os, Ru, Mn) are listed in Table 2, and the important distances therein, in Table 3. In addition, the existence of the isostructural $Sc_{\sim 19}Br_{28}Fe_4$ phase was established by powder data. These $Sc_{\sim 19}Br_{28}Z_4$ phases contain two basic

(14) Karcher, B. Ph.D. Dissertation, Iowa State University, Ames, IA, 1981.
(15) Walker, N.; Stuart, D. *Acta Crystallogr.* **1983**, *A39*, 158.
(16) Guloy, A. M.; Corbett, J. D. *Inorg. Chem.* **1996**, *35*, 4669.
(17) Whangbo, M. H.; Hoffmann, R.; Woodward, R. B. *Proc. R. Soc. London* **1979**, *366*, 23.

Table 3. Important Bond Distances (Å) in $Sc_{\sim 19}Br_{28}Z_4$ Phases

		$Sc_{18.9}Br_{28}Os_4$	$Sc_{19.0}Br_{28}Ru_4$	$Sc_{19.6}Br_{28}Mn_4$
Z−Z	(×3)	3.029(3)	3.077(4)	2.787(9)
Z−Sc1	(×3)	2.562(5)	2.537(4)	2.598(5)
Z−Sc2	(×3)	2.675(8)	2.676(5)	2.676(5)
Sc1−Sc1	(×2)	3.293(8)	3.284(5)	3.223(7)
Sc1−Sc1		3.64(1)	3.641(7)	3.597(8)
Sc1−Sc2	(×2)	3.512(4)	3.506(3)	3.475(4)
Sc1−Z		2.562(5)	2.537(4)	2.598(5)
Sc1−Br1	(×2)	2.795(4)	2.801(3)	2.796(4)
Sc1−Br1		3.021(5)	3.024(3)	3.038(4)
Sc1−Br2	(×2)	2.762(5)	2.747(3)	2.759(4)
Sc2−Sc1	(×6)	3.512(4)	3.506(3)	3.475(4)
Sc2−Sc2[a]	(×3)	4.31(2)	4.29(1)	4.42(1)
Sc2−Z	(×3)	2.675(8)	2.676(5)	2.676(6)
Sc2−Br1	(×3)	2.851(6)	2.848(4)	2.804(5)
Sc3−Sc3	(×3)	3.61(2)	3.66(1)	3.59(1)
Sc3−Br2	(×3)	2.855(9)	2.843(6)	2.836(7)
Sc3−Br3	(×3)	2.673(7)	2.684(5)	2.695(6)
Br1−Sc1		3.021(5)	3.024(3)	3.038(4)
Br1−Sc1	(×2)	2.795(4)	2.801(3)	2.796(4)
Br1−Sc2		2.851(6)	2.848(4)	2.804(5)
Br2−Sc1	(×2)	2.762(5)	2.747(3)	2.759(4)
Br2−Sc3		2.855(9)	2.843(6)	2.836(7)
Br3−Sc3	(×3)	2.673(7)	2.684(5)	2.695(6)
Br1−Br1[b]	(×2)	3.601(5)	3.616(3)	3.581(4)
Br1−Br2[b]	(×2)	3.699(2)	3.692(2)	3.664(3)
$\bar{d}_{Sc-Sc}$[a]		3.468	3.462	3.420

[a] Average over Sc_{16} cluster edges; Sc2−Sc2 not included. [b] All Br−Br distances ≤ 3.70 Å.

clusters units. One is a $Sc_{16}(Z)_4Br_{20}$ macrocluster or oligomeric unit, quite similar to those that have been previously refined as neutral units for $Y_{16}X_{20}Ru_4$ (X = Br, I), deduced for the isostructural $Sc_{16}Br_{20}Z_4$ (Z = Fe, Os) from powder data, and, with small halogen-bridging differences, established in $Y_{16}Br_{24}Ir_4$ and $Y_{16}Br_{24}Ir_4{\cdot}4YBr_3$.[1,2] In the present structure type, these oligomeric units are interbonded (via shared bromine atoms) with Sc_4Br_8 tetrahedral fragments, an arrangement previously seen only in $Gd_{20}I_{28}Mn_4$ where the tetrahedral units were concluded to function as nonreduced electron sources, viz., $Gd_4I_8^{4+}$.[3] (We defer a consideration of the fractional occupancy of the Sc3 atoms in the tetrahedron.) Geometric changes observed among the various $R_{16}Z_4$ cluster units as R, Z and the cluster electron counts vary, and the bonding changes inferred will be detailed later.

The metal portions in the primitive cubic cell of $Sc_{19}Br_{28}Z_4$ are illustrated in Figure 1, with $Sc_{16}Z_4$ oligomers at the origin and the Sc3 tetrahedron in the body center. (This and all subsequent figures utilize the positional and 90% probability anisotropic ellipsoids for the $Sc_{19.6}Br_{28}Mn_4$ structure.) Both units possess $\bar{4}3m$ (T_d) symmetry, the highest observed so far for any of the $R_{16}Z_4$ macroclusters. The larger unit is composed of two crystallographically unique scandium atoms, as illustrated in Figure 2. The Scl atoms, each of which is bonded to five other Sc atoms, define a truncated tetrahedron, while six-bonded Sc2 atoms cap the four pseudo-hexagonal faces thereon. The oligomers are oriented within the unit cell such that the 3-fold axes along the cell diagonals pass through the pseudo-hexagonal faces and the opposed Scl−Sc1−Sc1 truncated face of the imagined tetrahedral precursor. The smaller Sc_4 tetrahedra lie on the same rotation axes with its four vertices pointed toward the truncated faces of four $Sc_{16}Z_4$ clusters. Each oligomer can also be imagined to be the two-by-two condensation product of four distorted Sc_6Z octahedra, which are first joined to make pairs of edge-sharing octahedra and then further condensed.[2] The "octahedra" now appear as quite distorted trigonal anti-

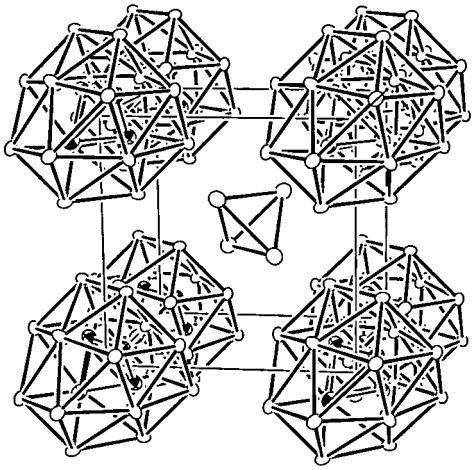

Figure 1. Cubic unit cell of $Sc_{\sim 19}Br_{28}Z_4$ phases, with oligomeric $Sc_{16}Z_4$ clusters at the corners and a Sc_4 tetrahedron at the body center. Br atoms are omitted for clarity; Z is quarter-shaded.

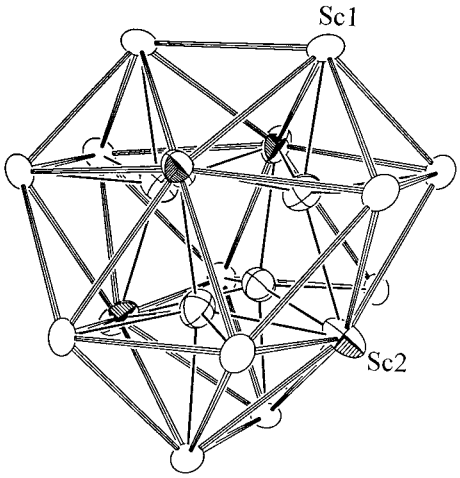

Figure 2. ~[$\bar{1}$00] view of the $Sc_{16}Z_4$ cluster unit, which possesses $\bar{4}3m$ (T_d) symmetry. The Sc1 atoms are open, Sc2 are quarter-shaded, and Z are crossed 90% ellipsoids.

prisms defined by Sc1−Sc1−Sc1 and Sc2−Sc2−Sc2 bases of quite different size. The interstitial atoms are also markedly shifted out of the centers of the "octahedra" toward the center of the macrocluster, although most Z−Z separations still remain relatively large.

Bond distances within the Sc_{16} oligomers, Table 3, are similar to those observed in other cluster halides. The Sc−Sc distances range from ~3.25 Å (Pauling bond order[18] (PBO) of 0.27) to ≥3.60 Å (PBO ≃ 0.05), with the shortest being the edges of the triangular Scl−Sc1−Sc1 faces. An intermediate ~3.50 Å separation appears within the nominally hexagonal faces, Sc2−Sc1, and the largest distances between neighboring atoms occur between pairs of apical Scl atoms (those bisected by the $\bar{4}$ axes along the cell edges) as well as between Sc3 atoms in the Sc_4 tetrahedra, which we will consider as largely nonbonding (3.60−3.66 Å). The formally shared edges of the imagined bioctahedral building blocks (Sc2−Sc2) are now much elongated, ~4.3 Å, and correlate with the displacements of Z. The average Sc−Sc distance in the oligomers, ~3.45 Å, is comparable to the distances observed in $Sc(Sc_6I_{12}Co)$, 3.39 and 3.49 Å,[8] but longer than those in $Sc_7Br_{12}C$, 3.21−3.30 Å.[4] However, these numbers are all heavily dependent on matrix effects, that is, on the sizes of the interstitials as these largely determine the cluster

(18) Pauling, L. *The Nature of the Chemical Bond*; Cornell University Press: Ithaca, NY, 1960; p 400.

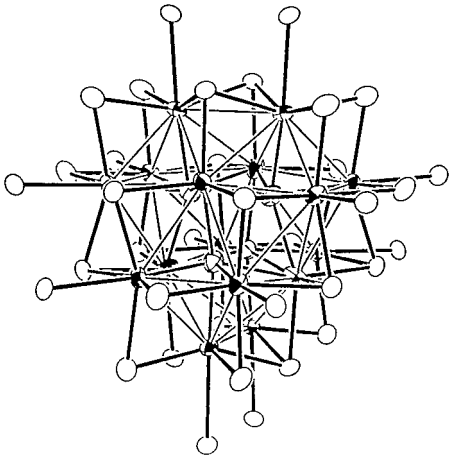

Figure 3. $Sc_{16}Z_4$ cluster (shaded and crossed ellipsoids) with its coordination sphere of 36 bromine atoms (open). Heavy lines emphasize the quasi-octahedral arrangement of Sc about Z.

radii and thence the surface distances. The lattice parameters and the cell volumes of the $Sc_{20-x}Br_{28}Z_4$ phases follow the trend Os > Ru >> Mn > Fe as predicted by Pauling's single bond radii, a comparison that presumes constant Sc−Br and Sc−Sc bond increments in the cell dimensions.

The Sc−Z distances for Z = Mn, Ru, Os vary from 2.47 to 2.60 Å with, surprisingly, *d*(Sc−Mn) the largest by ~0.04 Å, while distances within the Z_4 inner tetrahedra vary as Ru > Os >> Mn with PBO values between Z of 0.1l, 0.14, and 0.19, respectively. The Z−Sc2 distances are roughly 0.l Å greater than *d*(Z−Sc1) since the capping Sc2 atoms lie distinctly outside the Sc1 hexagons. Variations in the latter will be considered later along with the "breathing" distortions among a wider variety of oligomeric clusters. Generally, the Sc−Z distances are slightly smaller than the sum of Pauling's single bond metallic radii, a feature that has been observed in other cluster phases as well.

The internal dimensions of the $R_{16}X_{20}Z_4$ cluster units depend first on the size of the metal R. Thus, in the bromides the $Y_{16}Ru_4$ portion is larger in all respects than in $Sc_{16}Ru_4$, in $\bar{d}$(R1−R1) by 0.15 Å, in *d*(R1−Ru) by 0.16 Å, and in d(Ru-Ru) by a remarkable 0.28 Å. Crowding of larger iodine about $Y_{16}Ru_4$ (a matrix effect[19]) is presumably responsible for increases in $\bar{d}$(Y−Y) by 0.08 Å and *d*(Ru−Ru) by 0.19 Å relative to the bromide, without affecting *d*(Y−Ru). These oligomers as well as many smaller R_6Z examples very much give the impression of strong R−Z metal−metal interactions, while the rest of the distances are determined in major amount by these and, to lesser degrees, by R−R, Z−Z, and X−X interactions. Thus, the smaller Ru tetrahedron in $Sc_{16}Ru_4$ relative to $Y_{16}Ru_4$ in the bromides also appears to originate with a matrix effect from the size of R rather than a meaningful bonding change (below). On the other hand, a $Gd_{16}Mn_4$ vs $Sc_{16}Mn_4$ comparison is complicated by a greater breathing distortion in the former (vide infra), giving differences in *d*(R−Mn) and $\bar{d}$(R−R) of over 0.3 Å but only 0.04 Å in *d*(Mn−Mn). This effect also shows up in measures of the degree of the distortion of the R_6Z units on oligomer formation, such as the trans ∠Sc1−Ru−Sc2 angle (vertical in Figure 2) of 160° vs ∠Y1−Ru−Y2 of 166° and 170° in the bromide and iodide,[1,2] respectively, and 153° for ∠Sc1−Mn−Sc2.

As far as bromine roles, Figure 3 shows qualitatively how 36 bromine atoms sheath each $R_{16}Z_4$ unit. The approximately

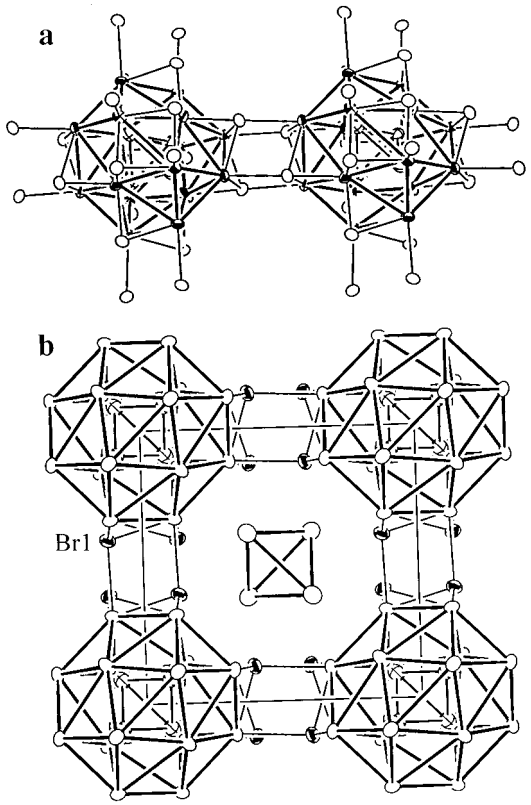

Figure 4. (a) Bonding mode of Br1 atoms (open ellipsoids), which cap three of the six Sc1−Sc1−Sc2 triangular faces on each hexagonal face of the Sc_{16} cluster. (b) Square network formed via complementary Br1 interconnections.

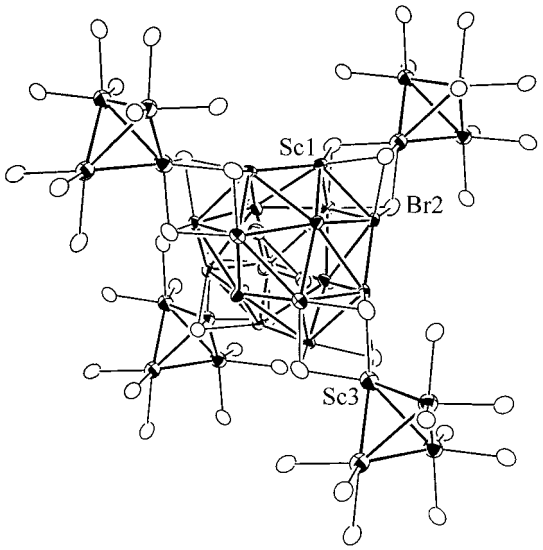

Figure 5. Bonding mode for Br2 (open ellipsoids), which bridges each Sc1−Sc1 edge of the oligomer and bonds (in groups of three) to Sc3 atoms in the tetrahedral fragment.

square array of Br1 and Br2 about each Sc1 vertex is seen to lie distinctly outside the metal center. There are three distinct modes of bromine bonding. Figure 4 pictures how Br1 atoms cap three alternate Sc1−Sc1−Sc2 triangular faces on each pseudo-hexagonal face and also bond exo to a Scl atom in an adjacent cluster. Each oligomer is thus connected to six neighboring oligomers related by unit cell translations. A second bridging mode with Br2 connects the oligomeric clusters to the Sc3 tetrahedra, Figure 5. Three Br2 atoms individually bridge Sc1−Sc1 edges (Br^i) of each Sc1−Sc1−Sc1 triangular face in the former while collectively bonding to a Sc3 vertex

(19) Corbett, J. D. In *Modern Perspectives in Inorganic Crystal Chemistry*; Parthé, E., Ed.; NATO ASI Series C; Kluwer Academic Publishers: Dordrecht, The Netherlands, 1992; pp 27−56.

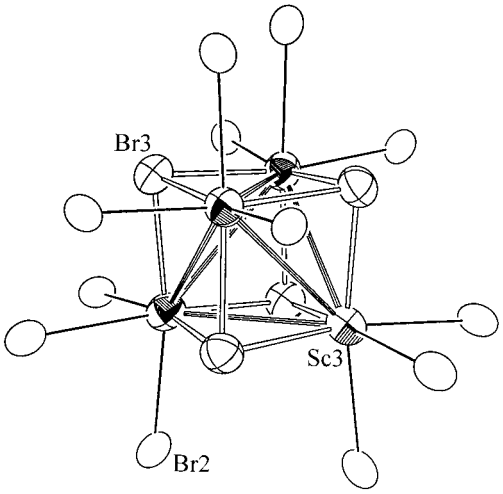

Figure 6. Tetrahedral Sc_4Br_8 fragment of Sc3 (72−89% occupied) with face-capping Br3 atoms and Br2 atoms that bridge to the $Sc_{16}Z_4$ clusters.

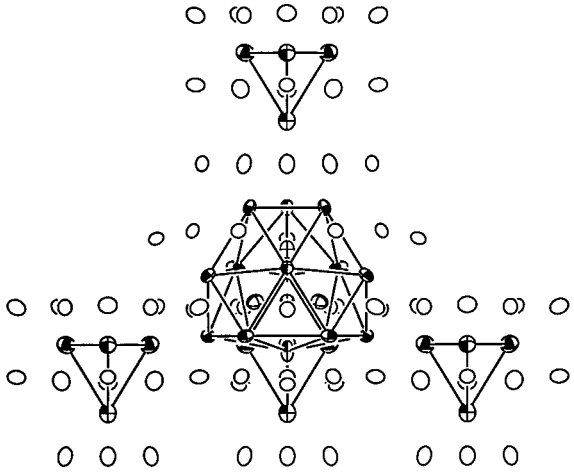

Figure 7. Sc_{16} cluster and neighboring Sc_{4-} fragments within layers of pseudo-close-packed Br and Z. Sc is quarter-shaded, Z is crossed, and Br is open.

(as Br^a) in the tetrahedron and vice versa from each tetrahedron to four oligomers via 12 $Br2^{a-i}$. The shortest intercluster Sc−Sc separation occurs here, 4.19 Å for Sc1−Sc3. The third bromine functionality is shown in Figure 6, Br3 atoms capping only the faces of the nominal $(Sc3)_4$ tetrahedron. The thermal ellipsoids for Br3 are characteristically larger, probably because of defects on the neighboring Sc3 positions (below). The ideal tetrahedral unit for now can be assigned as $(Sc3)_4(Br3)_4(Br2)_{12}\cdot 1/3 = Sc_4Br_8$. Similarly, the oligomic unit can be described as $(Sc1)_{12}(Sc2)_4(Z)_4(Br1^{i-a})_{12\cdot 2/3}(Br1^{a-i})_{12\cdot 1/3}(Br2^{i-a})_{12\cdot 2/3} = Sc_{16}Br_{20}Z_4$.

The Sc−Br bond distances around the macroclusters range from ∼2.75 to ∼3.04 Å, with the averages for the three compounds close to 2.83 Å. The edge-bridging Sc−Br2 atoms are the shortest, while the Br1 atoms exo to Sc1 vertices and *trans* to the interstitial atoms are the longest, as usual. The Sc3−Br2 distances around the Sc_4 tetrahedra are close to the average on the macrocluster. Distances to the face-capping, and only three-bonded, Br3 atoms are near 2.68 Å, a little shorter than the sum of crystal radii (2.705 Å)[20] and more typical of those about isolated Sc^{III} states.

The halogen and interstitial atoms collectively generate approximately cubic-close-packed layers, with each Sc atom in the large cluster occupying a pseudo-octahedral hole between the layers that is adjacent to one or three Z atoms, Figure 7. These layers lie parallel to (111), $(\bar{1}11)$, $(\bar{1}\bar{1}1)$, and $(11\bar{1})$ as do the four triangular faces of the Z_4 tetrahedra. The Sc3 atoms likewise occupy nearby sites defined only by Br atoms. Figure 7 shows that Z atoms are slightly displaced from midpoints between close-packed layers toward each other, while Sc atoms in the macrocluster are more noticeably shifted toward the center.

Cluster Electron Counts and Magnetic Susceptibilities. All of the $Y_{16}Z_4$ cluster units found earlier as well as the anion in $Gd_4I_8^{4+}(Gd_{16}I_{20}Mn_4^{4-})$ have 60 cluster-based (skeletal) electrons, a population that corresponds to a closed-shell manifold for both $Y_{16}I_{20}Ru_4$[1] and $Gd_{20}I_{28}Mn_4$[3] according to extended Hückel calculations. But structural refinements indicate that there are close to 61 skeletal electrons in $Sc_{19}Br_{28}Z_4$ (Z = Os, Ru), and the iron analogue identified only by its powder pattern is presumably similar. Localization of the odd electron in the macrocluster is expected according to results for all other paramagnetic halogen-bridged M_6Z clusters, and this is evidently what occurs (below). A 67% occupancy for Sc3 rather than the respective 72(3) and 74(2)% values refined would yield closed-shell $Sc_{18.67}Br_{28}$(Os,Ru) clusters with 60 skeletal electrons. Statistically, the former value cannot be distinguished from the observed ones at the 3.5σ level, but the magnetic properties confirm that these species are not closed shell.

The Sc3 vacancies are presumably present in order to reduce the nominal 64 skeletal electron count of stoichiometric $R_{20}X_{28}Z_4$ compounds (Z = Os, Ru (Fe)) toward the preferred 60 bonding electrons found in all other analogues. Random omission of about one-fourth of the Sc3 atoms in the small tetrahedron in these phases reduces the number of electrons available for cluster bonding from 64 to about 61, viz., $Sc_3Br_8^+(Sc_{16}Br_{20}Z_4^-)$. Apparently, the small tetrahedron will not tolerate the higher defect level necessary to give a closed-shell oligomer, which would be $Sc_{2.67}Br_8$. The structure of the parent $Gd_{20}I_{28}Mn_4$, which has four fewer electrons from Z, has a full Gd3 occupancy and thus the ideal 60 e oligomer. Also, there is no direct evidence for either twinning or a rhombohedral distortion in the present $Sc_{20-x}Br_{28}Z_4$ phases (in contrast to the behavior of $Gd_{20}I_{28}Mn_4$[3]) on the basis of the cubic refinement results. A slight rhombohedral distortion of the cell could conceivably allow ordering of the metal vacancy within the nominal $(Sc3)_4$ unit, but this should reduce the symmetry and possibly distort the oligomeric portion as well.

Magnetic susceptibility measurements were obtained for $Sc_{19}Br_{28}Os_4$, $Sc_{19}Br_{28}Ru_4$, and $Sc_{19}Br_{28}Fe_4$. These data are displayed as both molar susceptibility and its inverse as a function of temperature (K) in Figure 8. Interestingly, all three of the phases show two temperature domains, each of which exhibits an approximate Curie−Weiss type behavior, one above 100 K and the other below about 15 K. (Data for the iron compound were not analyzed because of impurities that were unaccounted for. Recall that M vs H data for the other two samples were examined, and the Ru member was corrected for ferromagnetic impurities—Experimental Section.) The effective moments and Weiss constants for each region in the ruthenium and osmium compounds are given in Table 4, column 2. The effective moments at low temperatures, 1.23 μ_B for both, are lower than expected for the spin-only values for one unpaired electron, but they are consistent with the moments observed for several other interstitially-stabilized rare-earth metal halide

(20) Shannon, R. P. *Acta Crystallogr., Sec. A* **1976**, *A32, 751.*

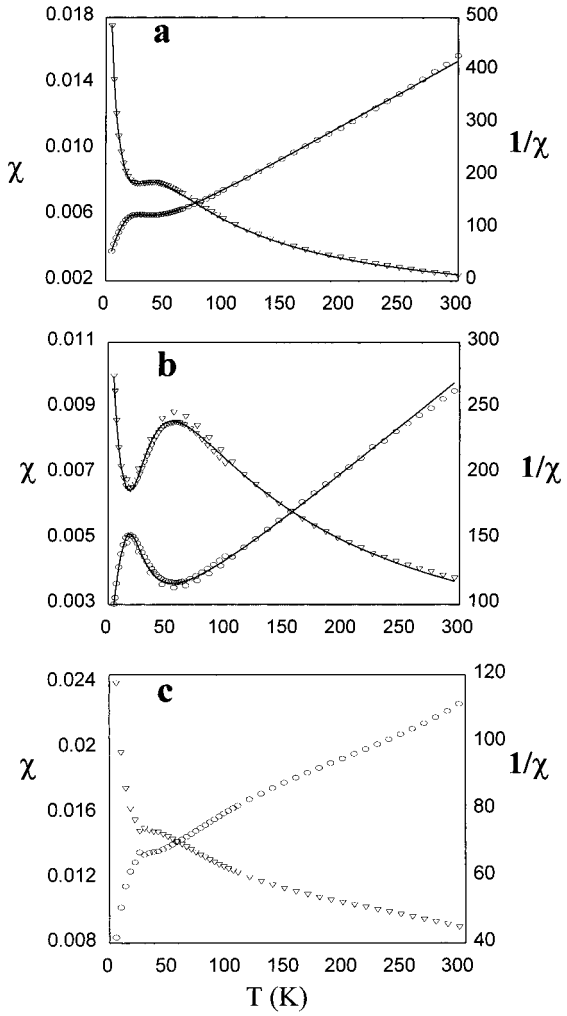

Figure 8. Observed molar magnetic susceptibilities, χ (triangles), and inverse susceptibilities, $1/\chi$ (ovals), as a function of temperature for (a) $Sc_{19}Br_{28}Ru_4$, (b) $Sc_{19}Br_{28}Os_4$, and (c) $Sc_{19}Br_{28}Fe_4$. The solid lines in a and b represent the calculated fit to the orbital crossing model.

clusters.[21,22] On the other hand, moments above 100 K, 2.5l and 3.45 μ_B, respectively, are much higher than expected on the basis of a simple one-electron spin-only model. The susceptibility behaviors around 60 K would ordinarily be associated with a reasonably strong antiferromagnetic coupling between paramagnetic clusters. However, such a coupling argument seems unlikely given that this system is magnetically quite dilute with only one unpaired electron per large cluster and direct center-to-center separations for these of ~11 Å, or 19 Å through the smaller tetrahedral clusters. A model consistent with the observed data will be discussed after a more detailed discussion of the unique bonding features in these clusters.

Magnetic properties of the manganese compound were not studied because the phase could not be obtained in high yield. Although this compound is isostructural and nominally isoelectronic with $Gd_{20}I_{28}Mn_4$, its X-ray refinement gave $Sc_{19.56(8)}Br_{28}Mn_4$ instead, the difference again arising entirely because of an evident ~89(2)% occupancy of the Sc3 site in the small tetrahedral cluster. The shortfall from $Sc_{20}Br_{28}Mn_4$ seems real with a difference of 5.5σ, and the reason for this is not understood.

(21) Lulei, M.; Martin, J. D.; Hoistad, L. M; Corbett, J. D. *J. Am. Chem. Soc.* **1997**, *119*, 513.
(22) Lulei, M.; Martin, J. D.; Corbett, J. D. *J. Solid State Chem.* **1996**, *125*, 249

Table 4. Fits of Magnetic Susceptibility Data for $Sc_{19}Br_{28}Z_4$ (Z = Ru, Os) at High and Low Temperatures to Curie−Weiss Behavior and Two Mixed $^2A_1$, $^2T_1$ Level Models

	Curie−Weiss fits	fit to orbital crossing model	fit to constant ΔE model[a]
	$Sc_{19}Br_{28}Ru_4$		
C_{low} ((emu·K)/mol)	0.19(1)	0.26(3)	0.169(1)
μ_{eff} (μ_B)	1.23	1.44	1.16
C_{high} ((emu·K)/mol)	0.788(8)	0.91(3)	1.59(1)
μ_{eff} (μ_B)	2.51	2.70	3.56
Θ_{low}	−6.2(4)	−6(3)	−4.7(1)
Θ_{high}	−32(2)	−25(4)	−119(14)
T_o (K)		65(7)	
m		1.5(2)	
n		12(5)	0.20(2)
R^2 (%)	99.1 (<15 K) 99.8 (>100 K)	99.99	99.97
	$Sc_{19}Br_{28}Os_4$		
C_{low} ((emu·K)/mol)	0.19(2)	0.41(6)	0.21(1)
μ_{eff} (μ_B)	1.23	1.81	1.30
C_{high} ((emu·K)/mol)	1.494(9)	1.58(6)	2.40(2)
μ_{eff} (μ_B)	3.45	3.55	4.38
Θ_{low}	−14.8	−28(6)	−12(10)
Θ_{high}	−100	−81(16)	−28(8)
T_o (K)		62(11)	
m		1.5(4)	
n		10(4)	13(21)
R^2 (%)	96.5 (<15 K) 99.99 (>100 K)	99.53	99.49

[a] $\Delta E = 1.03(1) \times 10^{-21}$ J for Ru, $1.07(2) \times 10^{-21}$ J for the Os phase.

Overview of Oligomer Characteristics. Exploratory synthetic investigations in Y−I−Z, Y−Br−Z, Gd−I−Z, and Sc−Br−Z systems have led to the identification of a new family of rare-earth metal halide cluster compounds stabilized by transition metal interstitials (Z), namely, with $R_{16}Z_4$ cluster units as building blocks. These fall into four structure types. Three types are built of only $R_{16}Z_4$ clusters coordinated and interbridged by halogens: (1) $Y_{16}I_{20}Ru_4$ and $Y_{16}Br_{20}Ru_4$, (2) $Y_{16}Br_{24}Ir_4$, and (3) $Y_{16}Br_{24}Ir_4{\cdot}4YBr_3$, all defined by single crystal structure studies, plus $Sc_{16}Br_{20}Z_4$ (Z = Fe, Os) identified as type 1 by Guinier powder diffraction data. The fourth structure type incorporates a second R_4X_8 cluster unit that is evidently not reduced but rather functions as a reducing agent. This type is found not only with electron-poorer Mn in $Gd_4I_8{\cdot}Gd_{16}I_{20}Mn_4$ but also for the substoichiometric $Sc_{\sim 3.6}Br_8{\cdot}Sc_{16}Br_{20}Mn_4$ and $Sc_{\sim 3.0}Br_8{\cdot}Sc_{16}Br_{20}Z_4$ for Z = Os, Ru. These types appear to be distinctly more common in the scandium and yttrium bromide systems than elsewhere.

The oligomers in all four structure types display a range of characteristic dimensional features and relationships. The basic sizes of the clusters, measured by $\bar{d}$(R−R) over the macrocluster, follow expectations according to standard metallic radii,[18] with Gd ≥ Y > Sc. The additional regular expansion caused by the larger iodine has already been noted. The same trend applies to $\bar{d}$(R−Z) as far as the size of Z except for the unusually large values with the electron-poorer Mn, viz., Mn > Os, Ir > Ru. The Gd−Mn member is also the only case in which d(R2−Z) becomes smaller than d(R1−Z). Distortions reflected in the cluster proportions appear to be a better way to sort out many of these effects and the accompanying bonding changes as well.

Geometric variations within the $R_{16}Z_4$ clusters can be characterized in a systematic manner in terms of regular "breathing" distortions of the type illustrated in Figure 9. These involve the contraction of the R1−R1−R1 triangular faces as the Z_4 tetrahedra get smaller, in concert with increases in the R2−R2 separations (those atoms capping pseudo-hexagonal faces of the truncated tetrahedron $R1_{12}$). The first three columns

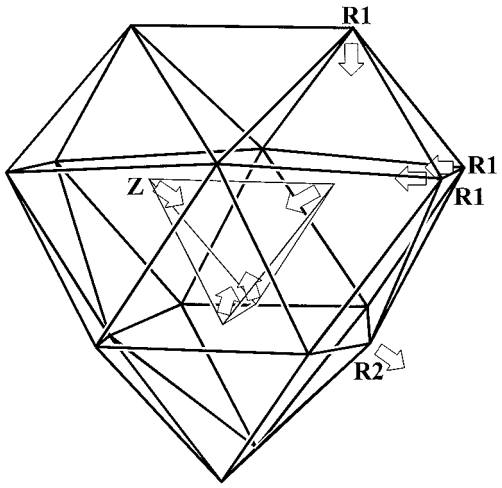

Figure 9. Concerted distortions characteristic of $R_{16}Z_4$ clusters, top to bottom in Table 4.

of data in Table 5 summarize in order of increasing distortion the metrical details for the eight oligomers now defined crystallographically. (The common atom numbering scheme is that of the $R_{20}X_{28}Z_4$ type, Figure 2.) These data alone are striking in how irregular the two electron-poorer manganese examples at the bottom of the table are. Were R1−Z distances to follow something like single bond metallic radii, then *d*(Sc1−Ru) should be about 0.07 Å greater than *d*(Sc1−Mn), not the 0.06 Å less that is observed. Likewise, *d*(R1−Mn) for Sc−Mn vs Gd−Mn should differ by ca. 0.18 Å, not the 0.39 Å observed. The remainder of Table 5 lists some ratios more appropriate to organizing the changing proportions of the oligomers: the ratios of (4) $\bar{d}$(R1−R1−R1) (abbreviated R1Δ) to *d*(R2−R2), which determine the order of the listing; (5) $\bar{d}$(R1−R1−R1) to Pauling's single bond metallic diameter d_1(R); (6) $\bar{d}$(R1−R1−R1) to $\bar{d}$(R−R) around the cluster (omitting the long second *d*(R2−R2)); and (7) *d*(Z−Z) to d_1(R). Also given are (8), the observed Z−Z PBO and (9) the *trans* R1−Z−R2 angle across R_6Z octahedra (Figure 2), which give an even clearer ordering than column 4, $\bar{d}$(R1Δ/$\bar{d}$(R2−R2). The angular measures reflect the regular displacement of the Z atoms toward the cluster center which also causes a general increase in R_2−R_2 separations since these atoms lie above the Z_4 faces, i.e., the breathing in Figure 9. The Z−Z distances relative to single bond metallic diameters (7), and the corresponding Pauling bond orders (8) follow almost the same trend.

Extended Hückel Calculations. To further our understanding of the bonding of this family of clusters, a series of extended Hückel MO calculations were performed on cluster units "$R_{16}X_{36}Z_4^{\ x-}$" derived from the crystal structures of $Gd_{20}I_{28}Mn_4$, $Sc_{20}Br_{28}Mn_4$, $Sc_{19}Br_{28}Ru_4$, and $Y_{16}I_{20}Ru_4$ with exo halogens added at the 16 vertices of each cluster. Results from calculations using a variety of H_{ii} parameters for both rare-earth and interstitial metals showed that significant variations depend mostly on whether Mn or Ru parameters are used for the interstitial element. The significant effects that the relative energies of the d orbitals of the rare-earth R vs those of the interstitial Z elements have on distortions in isoelectronic structures have recently been developed by Köckerling and Martin.[23] Structures containing interstitial elements such as Mn, for which the d orbital energies are comparable to those of the rare-earth elements, exhibit greater mixing of R and Z orbitals, and thus greater R-to-Z charge transfer, than for clusters with more electronegative interstitial elements. In the present calculations, utilization of Ru parameters results in rather well separated blocks of R−Z (lower) and R−R (higher) bonding orbitals, whereas the R−Z contributions are more evenly distributed throughout orbitals in the presence of Mn. As in the case of the monoclinic R_3X_3Z examples and their considerable range of distortions,[23] less charge transfer to the interstitial results in the less Z−Z bonding, consistent with the observed Z−Z distances.

While the relative orbital energies (electronegativities) of the rare-earth and interstitial elements are the major driving force behind the observed structural distortions, it is also useful to look from another perspective and consider the effects that the distortions have on the frontier molecular orbitals. In order to isolate the effects of metrical distortions on the cluster MO's from those originating with different energies for R and Z, a series of calculations was performed on the above four clusters utilizing Ru parameters for all of the interstitial elements, Y parameters for the Gd cluster (since the atoms are similar in size and ionization energies), and Sc parameters where present. The results are presented in Figure 10 according to the decreasing extent of distortion (left to right) as described in Figure 9 and Table 5 (bottom to top). A similar set of calculations was also made with Mn parameters throughout. The relative constancy seen for the lower occupied R−R bonding orbitals (t_2, e, and a_1) seems to reflect the reasonableness of the approximations since *d*(R−R) does not change significantly over the range of structures. By contrast, the frontier orbitals a_1 and t_1 (open bars), which contain significant R1−Z and R2−Z antibonding character, respectively, are dramatically affected by the cluster variations. As Z moves away from R1Δ and toward the R2−R2−R2 plane (right to left in Figure 10), the a_1 orbital loses R1−Z antibonding and becomes more Z−Z bonding and thus stabilized, while the t_1 orbital is destabilized by increased R2−Z antibonding effects. The larger Z inside the smaller Sc_{16} cage causes these trends to meet in the Ru and Os structures, such that the exact order predicted for the a_1 and t_1 orbitals is very sensitive to the input parameters. These general bonding trends are observed irrespective of what plausible orbital parameter sets are used. However, this a_1−t_1 orbital crossing takes place at an earlier stage within the distortion when Mn parameters are used (i.e., closer to the $Y_{14}I_{20}Ru_4$ cluster dimensions). The use of Mn parameters also reduces the gap between the 60-electron HOMO and the a_1 LUMO, particularly in the Gd structure, such that it is not certain from these calculations whether $Gd_{20}I_{28}Mn_4$ is closed shell.

Bonding and Magnetism. Finally, it is worthwhile to consider how this bonding picture relates to the observed magnetic properties of these clusters, and in particular, whether the calculated "orbital-crossing" picture could be responsible for the observed temperature dependence of the magnetic susceptibilities, Figure 8. In $Sc_{19}Br_{28}Z_4$ (Z = Ru, Os, Fe), about one unpaired electron per macrocluster populates either the a_1 or t_1 orbital depending on their relative energies. Since the two MO's may be separated by energies of the order of *kT*, we must consider both when interpreting the magnetic properties. The states $^2T_1$ and $^2A_1$ resulting from one electron in the t_1 or a_1, respectively, look similar in a first approximation to the term symbols describing the states of transition-metal ions. To our knowledge, there has been no detailed theoretical attempt to explain magnetic properties of transition (and inner-transition) metal clusters to the same level that ligand field theory has achieved for transition metal ion complexes. Therefore, we start our discussion from a simple consideration of the orbital angular momentum of states.

(23) Köckerling, M.; Martin, J. D. To be submitted for publication.

Table 5. Pertinent Distances (Å), Ratios, Bond Orders, and Angles (deg) That Are Helpful in Understanding the Trends in and Distortions of $R_{16}Z_4$ Clusters

	$\bar{d}_{R-R}$ (1)	$\bar{d}_{R1-Z}$[a] (2)	d_{R2-Z}[a] (3)	$\bar{d}_{R1\Delta}/\bar{d}_{R2-R2}$ (4)	$\bar{d}_{R1\Delta}/d_1(R)$[b] (5)	$\bar{d}_{R1\Delta}/\bar{d}_{R-R}$ (6)	$\bar{d}_{Z-Z}/d_1(Z)$ (7)	PBO_{Z-Z} (8)	∠R1−Z−R2 (9)
$Y_{16}I_{20}Ru_4$[c]	3.76	2.69	2.83	0.842	1.125	0.967	1.433	0.02	169.57(5)
$Y_{16}Br_{20}Ru_4$[d]	3.69	2.70	2.82	0.813	1.113	0.976	1.348	0.04	165.52(9)
$Y_{20}Br_{36}Ir_4$[d]	3.73	2.74	2.83	0.814	1.133	0.983	1.326	0.04	164.3(2)
$Y_{16}Br_{24}Ir_4$[d]	3.72	2.75	2.83	0.806	1.124	0.976	1.310	0.05	163.9(2)
$Sc_{19.0}Br_{28}Ru_4$	3.46	2.54	2.68	0.766	1.141	0.949	1.235	0.11	160.5(2)
$Sc_{18.9}Br_{28}Os_4$	3.47	2.56	2.68	0.764	1.144	0.950	1.202	0.14	159.3(2)
$Sc_{19.6}Br_{28}Mn_4$	3.42	2.60	2.68	0.729	1.120	0.942	1.183	0.19	153.2(3)
$Gd_{20}I_{28}Mn_4$[e]	3.76	2.99	2.92	0.730	1.103	0.952	1.200	0.16	148.3(2)

[a] As R1 and R2 are differentiated in the $R_{20}X_{28}Z_4$ structure type. [b] d_1 is the single bond metallic diameter.[19] [c] Reference 1. [d] Reference 2. $Y_{20}Br_{36}Ir_4$ is $Y_{16}Br_{20}Ir_4 \cdot 4YBr_3$. [e] Reference 3.

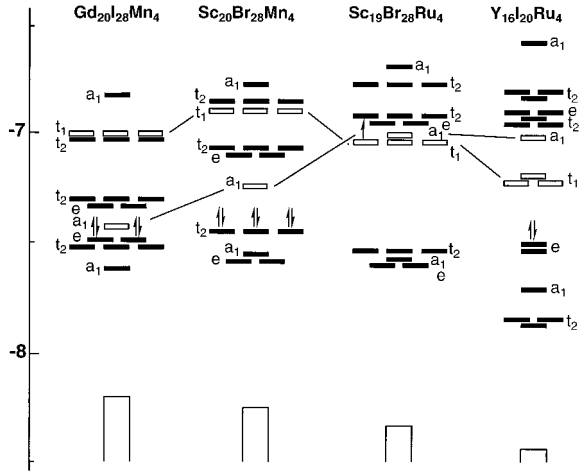

Figure 10. Cluster-based MO's for $R_{16}X_{36}Z_4$ clusters with, left to right, decreasing distortions in the sense of Figure 9 (see the text for the simplifications employed). Note the course of the a_1 and t_1 frontier MO's as a function of distortion. (The symmetry labels used for $Y_{16}I_{20}Ru_4$ are the idealized tetrahedral values.)

To a first approximation, the triply degenerate T_1 is considered to have orbital angular momentum $L = 1$, as with p-orbitals, and the nondegenerate A_1 to have $L = 0$. Because of the additional contribution of the orbital angular momentum, a higher effective magnetic moment is expected for $^2T_1$ than for $^2A_1$. Based on a free ion model,[24,25] $\mu_{eff} = g(J(J+1))^{1/2}$, and one calculates according to the usual Russell−Sanders coupling scheme effective moments of 1.73 μ_B for $S = {}^1/_2$, $L = 0$ and 2.57 μ_B for $S = {}^1/_2$, $L = 1$.[26] These values bear a striking parallel to those obtained from separate Curie−Weiss fits to the low-temperature and high-temperature magnetic data for the Ru and Os clusters, respectively (Table 4). Furthermore, as the extended-Hückel calculations demonstrate, the relative positions of the frontier molecular orbitals are extremely sensitive to small distortions in the crystal structure. Contraction of the unit cell dimensions expected upon cooling the crystalline solid is likely to slightly favor a distortion in the direction of the contracted cluster (as in Figure 9), which is also the direction that is predicted to stabilize the a_1 orbital. Based on the above reasoning and the observed trends, it seems reasonable to predict that the magnetic orbital (the orbital which contains the unpaired electron) in $Sc_{19}Br_{28}Z_4$ (Z = Ru, Os, Fe) clusters is the a_1 orbital at low temperature whereas it is t_1 at higher temperatures. And, thus, while the magnetic susceptibility is determined by a Boltzman distribution over all states, this distribution is statistically weighted by the state derived from the magnetic orbital.

To test the two-state hypothesis, irrespective of the above expectations, we have constructed a temperature-dependent model that beautifully fits the observed data. This model came from the basic recognition that, ignoring the spin−orbit coupling between $^2T_1$ and $^2A_1$, the magnetic moments from the two states are independent of each other and that the population of the states is governed by a Boltzmann distribution. The magnetic susceptibility, χ, of each state can be expressed as $\chi = C/(T - \Theta)$, where C is the Curie constant and Θ reflects the deviation from Curie behavior. Because of the magnetic diluteness of the systems, we do not expect Θ to result from significant intercluster magnetic coupling; rather, it is likely to be determined by the population of two levels close in energy. (These may also be significantly influenced by spin−orbit coupling,[24,25] which we do not attempt to treat.) By including thermal effects in the total magnetic susceptibility via a Boltzmann distribution, we propose that

$$\chi = \left(\frac{C_{low} + C_{high}e^{-\Delta E/kT}}{1 + e^{-\Delta E/kT}}\right)1/(T - \Theta) \qquad (1)$$

where

$$\Theta = \left(\frac{\Theta_{low} + \Theta_{high}e^{-\Delta E/kT}}{1 + e^{-\Delta E/mkT}}\right) \qquad (2)$$

k is the Boltzmann constant, and m is a constant possibly related to spin−orbit coupling. We now simply model the ΔE by a linear function with a scaling factor n and T_o as the temperature of the orbital crossing ($\Delta E = 0$), such that ΔE is positive for a_1 below t_1, i.e.,

$$\Delta E = nk(T_o - T) \qquad (3)$$

This is clearly an overly simplistic model for ΔE, but the model is usable over the temperature range examined with a maximum ΔE of 5×10^{-21} J at 300 K (0.03 eV, coincidentally a value of the same magnitude as obtained in the extended Hückel calculations).

The remarkable fits of the measured data for the Ru and Os clusters to the above function are shown in Figure 8 as the solid lines ($R^2 = 99.99$ and 99.53%, respectively) with the extracted values for C and Θ listed in Table 4. It is interesting to note that the values of Θ are significantly larger for the Os cluster than those observed for the Ru cluster, consistent with the expectation of greater spin−orbit coupling for the heavier interstitial element. The deviations of the effective moments from the expected low-temperature (1.73) and the high-

(24) Carlin, R. *Magnetochemistry*; Springer-Verlag: Berlin, 1986.
(25) Mabbs, F. E.; Machin, D. J. *Magnetism and Transition Metal Complexes*; Chapman and Hall: London, 1973.
(26) A free-ion model in which spin−orbital coupling is small with respect to kT, $\mu_{eff} = [L(L+1) + 4S(S+1)]^{1/2}$, gives a somewhat smaller $\mu_{eff} = 2.24\ \mu_B$ for the $S = {}^1/_2$, $L = 1$ state: Earnshaw, A. *Introduction to Magnetic Chemistry*; Academic Press: New York, 1968; Chapter 2.

temperature (2.57) values may be indicative of an occupancy of other than 75% for the R3 atoms. However, these deviations are more likely to be a result of limitations to the free-ion predictions and because of the incomplete treatment of spin−orbit effects.

The outstanding fits obtained with reasonable values for C, Θ, and ΔE show that the proposed model is consistent with the observed data; however, it in no way proves that the model is correct. We can model the data nearly as well by assuming a constant value for ΔE, i.e., no orbital crossing (last column, Table 4). Here, too, the effective moment is expected to increase as kT approaches and exceeds ΔE if the a_1 orbital is slightly below the t_1. This case is somewhat analogous to the enhanced effective moment observed in magnetic metals that exhibit a high density of states because of narrow bands at the Fermi level, known as the Stoner enhancement.[27,28] However, the model is not our favored explanation for the data because it is difficult to account for the more extreme effective moments at high temperature. We have also considered the possibility that the observed data are simply a result of spin−orbit coupling of a $^2T_1$ ground state plus a small ferromagnetic impurity. While derivation of the wave function for the t_1 cluster orbital is nontrivial, the observed maximum in the plot of $1/\chi$ vs T seems inconsistent with the spin−orbital coupling described for $^2T_2$ octahedral Ti(III) complexes[24,25] and with the $^2T_{2g}$ ground state of $Zr_6I_{12}Mn$.[29] Note that ferromagnetic impurities were also examined in the data workup.

The proposed "orbital crossing" model that so nicely accounts for the observed magnetic behavior of the $Sc_{19}Br_{28}Z_4$ clusters is a consequence of both the extreme sensitivity of the frontier molecular orbitals to small changes in the metrical parameters of the cluster and the presence of orbitals with differing orbital angular momentum, separated by $\Delta E \approx kT$, in the immediate vicinity of the HOMO−LUMO gap. While the former may be relatively unique to the clusters at hand, the latter phenomenon is expected to occur in large paramagnetic clusters (or nanoparticles) with high symmetry and delocalized frontier molecular orbitals.

Acknowledgment. The authors thank Victor Young for maintenance of the diffractometers and Jerry Ostenson for measurements of the magnetic data. J.D.M. gratefully acknowledges D.-K. Seo for many helpful discussions pertaining to the interpretation of the magnetic data and Dr. D. Boos for assistance with fitting the data. This research was supported by the National Science Foundation, Solid State Chemistry, via Grants DMR-9207361 and -9510278 and was carried out mainly in the facilities of the Ames Laboratory, U. S. Department of Energy.

Supporting Information Available: Tables listing additional crystallographic data, anisotropic displacement parameters, and angles in the three structures (4 pages). Ordering information is given on any current masthead page.

IC970881J

(27) Cox, P. A. *Transition Metal Oxides;* Oxford University Press: Oxford, U.K., 1992.

(28) Gubanov, V. A.; Liechtenstein, A. I.; Postnikov, A. V. Magnetism and the Electronic Structure of Crystals. *Solid-State Sciences*; Springer-Verlag: Berlin, 1992; Vol. 98.

(29) Hughbanks, T.; Rosenthal, G.; Corbett, J. D. *J. Am. Chem. Soc.* **1988**, *110*, 1511.